Journal of Alloys and Compounds 509 (2011) 2729–2733

Contents lists available at ScienceDirect

Journal of Alloys and Compounds

journal homepage: www.elsevier.com/locate/jallcom

The ternary iron aluminum carbides

J.A. Jiménez [a,*], G. Frommeyer [b]

[a] Department of Physical Metallurgy, Centro Nacional de Investigaciones Metalúrgicas, C.S.I.C., Av. Gregorio del Amo 8, 28040 Madrid, Spain
[b] Department of Materials Engineering, Max Planck Institut für Eisenforschung, Max Planck Str. 1, 40237 Düsseldorf, Germany

ARTICLE INFO

Article history:
Received 20 May 2010
Received in revised form 1 December 2010
Accepted 3 December 2010
Available online 10 December 2010

Keywords:
Iron aluminum carbides
X-ray diffraction
Rietveld method

ABSTRACT

Carbides present in ternary Fe–Al–C were investigated by the combined utilization of an X-ray diffractometer and a scanning electron microscope equipped with an energy dispersive X-ray spectrometer. The alloys were prepared by arc melting and the microstructure was homogenised by a solution annealing treatment in the temperature range 950–1050 °C for 15 min. The diffraction patterns of resulting materials were analysed using a multiphase Rietveld refinement. The steel is composed of a ferritic matrix with carbides Fe_3C, $M_{23}C_6$, and/or κ-Fe_3AlC depending on the Al and C concentration. It is the first time that the existence of $M_{23}C_6$ ternary carbide in the Fe–Al–C system is recognized. Microprobe analyses performed revealed that the solubility of Al in $M_{23}C_6$ is low, with an Fe/Al ratio (in at.%) higher than 15. On the other hand, the amount of Al in the cementite is negligible and hence its lattice parameters do not depend on the Al concentration of the alloy.

1. Introduction

The Fe–Al–C system is of interest in the development of low cost permanent magnetic alloys, which are suitable replacements for some cobalt steels and also may be of use in situations where easy reversal of polarity is required [1,2]. Recently, attention has also been drawn to decrease the weight of structural parts and increase the corrosion resistance by the addition of Al to steel [3,4]. The lower weight (26.981) and higher radius (143 pm) of Al atoms when compared to weight (55.847) and radius (124 pm) of Fe atoms yield to a density reduction. On the other hand, the formation of a surface aluminum oxide film improves the steel corrosion resistance. In most of the reported literature of Fe–Al alloys for structural applications the carbon contents is very low (<0.05 wt.%), because carbon is believed to result in a significant loss in ductility [5]. However, a few authors have shown that addition of carbon to binary alloys with an Al content ranging from 8.5 to 16 wt.% resulted in greatly improved elevated temperature strength and creep resistance, without a significant reduction in ductility [6–9]. This is attributed to precipitation hardening by formation of a uniform distribution of fine carbides.

Phase equilibria in the Fe–Al–C system near the Fe corner have been investigated extensively [10–15]. At low C content, these alloys are characterized by a wide α-Fe solid solution having a body-centered cubic (BCC) crystal structure. For aluminum content above 18 at.% (9.3 wt.%) a brittle intermetallic phase is formed. Then, the attention is directed to the lower Al end of the phase diagram. At high C content, the face-centered cubic (FCC) crystal structure is stable and a ternary carbide, denoted as κ-phase or κ-carbide, exists. This carbide, with the Strukturbericht $E2_1$, can form a eutectoid structure with α-Fe in the same way as cementite when austenite is cooled. The $E2_1$ structure, also known as perovskite, is an ordered $L1_2$-type structure based on the FCC lattice with Al at the cube corners and Fe on the cube faces and a carbon atom in the central octahedral site. A prefect arrangement of this type would correspond to the composition Fe_3AlC, but this stequiometry has never been observed. The κ-carbide is represented by the formula, Fe_3AlC_x, where x can varies from 0.5 to 1, and its lattice parameter can vary from 0.372 nm to 0.378 nm with increasing carbon concentration [16–18].

The aim of the present work was to determine the nature of carbides in Fe–Al–C alloys and correlated it with the concentration of Al and C. For this task, several Fe–*X*Al–1C, with *X* ranging from 2 to 6 wt.%, and Fe–6Al–YC, with Y ranging from 1.2 to 1.8 wt.%, were prepared and after homogenisation X-ray diffraction experiments were carried out. According to the vertical sections at a constant carbon concentrations reported by Palm et al. [14], the alloys with C concentration of 1 wt.% (~4.3 at.%) and Al content up to ~5 wt.% (~9.5 at.%) should be included in the α + graphite region and for higher Al content in the α + κ + graphite region. On the other hand, all the alloys of the Fe–6Al–YC should be included in the three phases (α + κ + graphite) region.

2. Experimental procedure

Steels were prepared by vacuum arc melting from pure iron (99.97%), aluminum (99.99%) and graphite. The chemical compositions are listed in Table 1.

* Corresponding author. Tel.: +34 91 5538900; fax: +34 91 5347425.
E-mail address: jimenez@cenim.csic.es (J.A. Jiménez).

0925-8388/$ – see front matter © 2010 Elsevier B.V. All rights reserved.
doi:10.1016/j.jallcom.2010.12.017

Table 1
Chemical composition of alloys.

Alloy	Fe	Al (wt.%)	Al (at.%)	C (wt.%)	C (at.%)
Fe–2Al–1C	Bal.	2	3.91	1	4.40
Fe–3Al–1C	Bal.	3	5.81	1	4.35
Fe–4Al–1C	Bal.	4	7.67	1	4.31
Fe–5Al–1C	Bal.	5	9.50	1	4.27
Fe–6Al–1C	Bal.	6	11.28	1	4.22
Fe–6Al–1.2C	Bal.	6	11.21	1.2	5.04
Fe–6Al–1.4C	Bal.	6	11.14	1.4	5.84
Fe–6Al–1.8C	Bal.	6	10.99	1.8	7.41

Microstructure of these steels was homogenised by a thermal treatment. This heat treatment was characterized by solution annealing at 950–1050 °C for 15 min with air quenching to room temperature and a following tempering treatment at 500 °C for 15 min.

Microstructure present in the alloys after these heat treatments was characterized using X-ray diffraction and a scanning electron microscope equipped with an energy dispersive X-ray spectrometer, EDS. Standard grinding and polishing techniques were used for these studies, and a final polish with 1 μm diamond paste and colloidal silica (40 nm) to remove the deformed layer. In order to estimate the chemical composition of different phases, EDS semiquantitative analyses were performed. Due to the very small size of the carbides in some samples, a microprobe measuring point could include large part of ferritic matrix around them. The result obtained in these cases has been just used for qualitative purpose, to determine differences between the phases present in the microstructure.

X ray diffraction measurements were carried out with a Bruker AXS D8 diffractometer equipped with X-ray Co tube and Goebel mirror optics to obtain a parallel and monochromatic X-ray beam. A current of 30 mA and a voltage of 40 kV were employed as tube setting. Operational conditions were selected to obtain X-ray diffraction diagrams of sufficient quality: sufficient counting statistics, narrow peaks and detection of small diffraction peaks of minor phases. XRD data were collected over a 2θ range of 20–115° with a step width of 0.03° and a counting time of 10 s/step.

It is well known that the Rietveld method is a powerful tool for calculation of structural parameters from diffraction patterns of polycrystalline bulk materials recorded in Bragg–Brentano geometry. The application of the Rietveld method to the patterns taken under the diffractometer set-up used requires consideration of all the peculiarities of this technique causing significant deviations from the intensities recorded in Bragg–Brentano geometry. In order to take in account such particularities in the Rietveld refinement, instrument functions were empirically parameterised from the profile shape analysis of a corundum sample measured under the same conditions. In this study, we have used the version 4.0 of Rietveld analysis program TOPAS (Bruker AXS) for the XRD data refinement. The refinement protocol included also the background, zero displacement, the scale factors, the peak breath, the unit cell parameter and texture parameters. The quality and reliability of the Rietveld analysis were quantified by the corresponding figures of merit: the weighted summation of residual of the least squares fit, R_{wp}, the statistically expected least squares fit, R_{exp}, the profile residual, R_p, and the goodness of fit (sometimes referred as Chi-squared), GoF [19]. Since $GoF = R_{wp}/R_{exp}$, a GoF = 1.0 means a perfect fitting.

The room temperature structures used in the refinement were ferrite and, depending on Al and C concentration, an appropriated combination of the carbides Fe_3C, $M_{23}C_6$, and κ-Fe_3AlC. Ferrite was described with an atomic distribution corresponding to the composition measured in the microprobe analyses.

The M_3C carbide crystallizes in the orthogonal system (space group Pnma) with four formula units ($Z = 4$) per unit cell, where eight metal atoms (M(g)) are in "general" positions (8d), four metal atoms (M(s)) in "special" positions (4c), and four carbon atoms in the interstices [20]. We obtained in the microprobe measures very low content of Al for this carbide, thus the structure description of pure Fe_3C was kept.

The $M_{23}C_6$ carbide crystallizes in a cubic face-centered (space group *Fm*-3*m*) in which 92 metal atoms are located at the 4(a), 8(c), 32(f), and 48(h) symmetry sites. Carbon atoms are placed on 24(e) sites [21]. Concerning the repartition of the elements in the crystallographic sites, the paper of Xie at al. [22] provided the following information: the large (molybdenum and tungsten) atoms tend to be found exclusively on 16-coordinated 8(c) sites. Since Al atomic radius (143 pm) is even higher than that for Mo and W (139 pm), Al atoms were placed at this site. The geometrically close-packed 4(a) and the sites bonded to carbon atoms, 48(h) and 32(f), are less favourable for iron substitution. Starting from these data, site occupancies were adjusted for Fe, and Al atoms in order to take account of the real composition measured by microprobe analysis: a Fe/Al ratio (in at.%) of 15 for the Fe–3Al–1C. Although the Al content might be a bit lower for the Fe–2Al–1C alloy or higher for the Fe–4Al–1C and Fe–5Al–1C, this ratio was kept for all data sets of diffraction patters.

Finally, the κ-Fe_3AlC carbide crystallizes in a cubic primitive lattice (Pm-3m) in which Fe and Al atoms are located at the 3(c) and 1(a) symmetry sites, respectively. Carbon atoms are place on the 1(b) site [18]. Pronounced non-stoichiometry is well known for the k phase in the Fe–Al–C system and the Site Occupancy Factor (SOF) for C can vary from 0.5 to 1.0. In this work, the SOF was refined during the Rietveld analysis of the different samples.

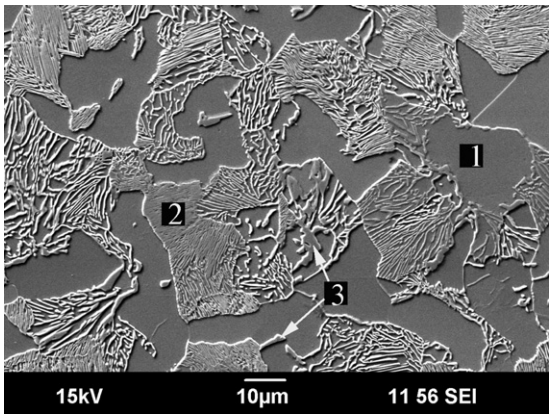

Fig. 1. Scaninng electron micrograph showing the microstructure presents in the Fe–2Al–1C alloy. Features: (1) ferrite, (2) laminar pearlite and (3) grain boundary carbide.

3. Results

3.1. Fe–2Al–1C and Fe–3Al–1C

Microstructure of Fe–2Al–1C and Fe–3Al–1C alloy is quite similar. Fig. 1 shows a micrograph of the Fe–2Al–1C alloy. This figure shows the presence of ferrite, lamellar pearlite and some carbides at the grain boundaries. Semiquantitative microanalysis performed in ferrite indicates an aluminum concentration slightly higher than the nominal composition of the alloy, 2.6 and 3.7 wt.%, respectively. These values correspond to a Fe/Al atomic ratio of 18.2 and 12.5, respectively. In the case of grain boundaries carbides, only the Fe/Al atomic ratio was determine, since the accuracy of carbon quantification is poor with the SEM-EDS system used. A value of 19.8 and 15.2 was obtained for the Fe–2Al–1C and Fe–3Al–1C, respectively. Due to the small size of the carbide in pearlite, the microanalysis measurements performed include information of the ferrite around them. However, the value for the ratio between the Fe and Al concentration was used to compare the Al concentration in both type of carbide. A value of 21.9 and 20.6 for the Fe/Al atomic ratio was measured, which is lower that that measured in both, ferrite and grain boundaries carbides.

Fig. 2 shows the results of the Rietveld analysis. This figure shows that apart from those phase that existed in the Fe–2Al–1C alloy, κ-carbide diffraction peaks, indicated by arrows, are also present in the Fe–3Al–1C alloy. The lattice parameters and mass fraction of the phases optimized in this refinement are presented in Table 2. Instead the graphite predicted in the phase diagram, the alloys presents two carbides: Fe_3C and $(Fe,Al)_{23}C_6$. Ferrite mass fraction is almost the same for both alloys, but the increase in Al content leads to appearance of some κ-carbide and the decrease of relative content of $(Fe,Al)_{23}C_6$.

3.2. Fe–4Al–1C, Fe–5Al–1C and Fe–6Al–1C

The increase of the Al content in the Fe–*X*Al–1C system makes the microstructure to evolve from a microstructure similar to those present in Fig. 1 in the alloy Fe–4Al–1C, to the nearly spheroidized pearlite structure in a ferrite matrix shown in Fig. 3 for the Fe–6Al–1C alloy. Microstructure of Fe–5Al–1C alloy is more complex and difficult to interpret. It is included lamellar pearlite, fine spherical carbide, and some grain boundaries carbides in a matrix of ferrite, as observed at higher magnifications in Fig. 4.

Table 2
Results of Rietveld X-ray diffraction pattern refinement for Fe–XAl–YC alloys.

Alloy	Phase	Space group	*a* (nm)	*b* (nm)	*c* (nm)	Mass fraction	*X* in Fe_3AlC_x
Fe–2Al–1C	α-Fe	$Im\bar{3}m$	0.2875			84.1%	
	$(Fe,Al)_{23}C_6$	$Fm\bar{3}m$	1.0541			8.8%	
	Fe_3C	Pnma	0.5078	0.6746	0.4517	7.1%	
Fe–3Al–1C	α-Fe	$Im\bar{3}m$	0.2878			84.3%	
	$(Fe,Al)_{23}C_6$	$Fm\bar{3}m$	1.0545			6.5%	
	Fe_3C	Pnma	0.5082	0.6749	0.4520	8.5%	
	κ-Carbide	$Pm\bar{3}m$	0.3790			0.7%	
Fe–4Al–1C	α-Fe	$Im\bar{3}m$	0.2881			84.5%	
	$(Fe,Al)_{23}C_6$	$Fm\bar{3}m$	1.0550			1.0%	
	Fe_3C	Pnma	0.5086	0.6750	0.4524	9.0%	
	κ-Carbide	$Pm\bar{3}m$	0.3790			5.5%	0.93
Fe–5Al–1C	α-Fe	$Im\bar{3}m$	0.2882			81.7%	
	$(Fe,Al)_{23}C_6$	$Fm\bar{3}m$	1.0549			3.2%	
	Fe_3C	Pnma	0.5087	0.6750	0.4526	4.5%	
	κ-Carbide	$Pm\bar{3}m$	0.3790			10.6%	0.99
Fe–6Al–1C	α-Fe	$Im\bar{3}m$	0.2883			84.9%	
	Fe_3C	Pnma	0.5080	0.6751	0.4528	1.1%	
	κ-Carbide	$Pm\bar{3}m$	0.3789			14.0%	1.00
Fe–6Al–1.2C	α-Fe	$Im\bar{3}m$	0.2881			75.5%	
	κ-Carbide	$Pm\bar{3}m$	0.3784			24.5%	0.80
Fe–6Al–1.4C	α-Fe	$Im\bar{3}m$	0.2880			73.6%	
	κ-Carbide	$Pm\bar{3}m$	0.3785			26.3%	0.77
	Graphite	P63/mmc	0.2404		0.6710	0.1%	
Fe–6Al–1.8C	α-Fe	$Im\bar{3}m$	0.2881			73.9%	
	κ-Carbide	$Pm\bar{3}m$	0.3783			25.7%	0.76
	Graphite	P63/mmc	0.2403		0.6710	0.4%	

Fig. 5 and Table 2 show the results of the Rietveld analysis. An Al content increase from 4 to 6 wt.% it is accompanied a progressive increase of intensity of κ-carbide diffraction peaks, indicated by arrows in Fig. 5, and the disappearance of the peaks corresponding to both, Fe_3C and $(Fe,Al)_{23}C_6$ carbides. As present in Table 2, the mass fraction κ-carbide ranges from 5.5 to 14.0% for the alloy with 4 and 6 wt.% Al, respectively. At the same time, only 1.1% Fe_3C was calculated for the Fe–6Al–1C alloy.

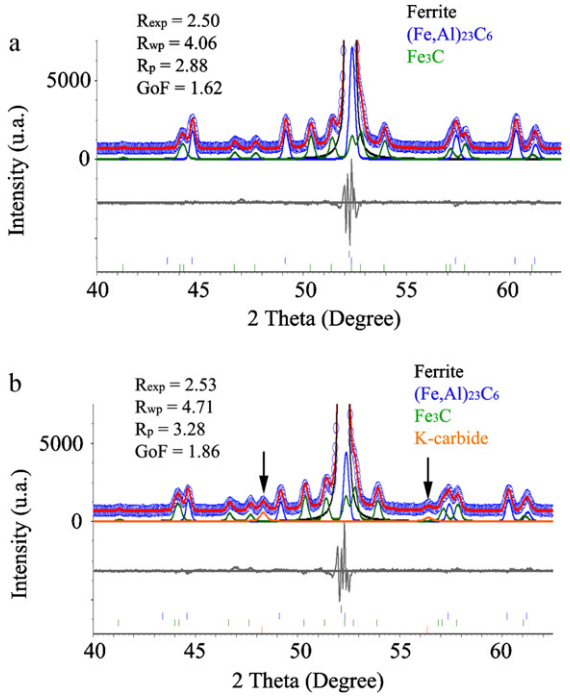

Fig. 2. Observed (hollow circles) and Rietveld fitted (solid line) X-ray diffraction patterns for the (a) Fe–2Al–1C and (b) Fe–3Al–1C alloys. The difference between the experimental data and the fitted simulated pattern is shown as a continuous line under the diffraction patterns.

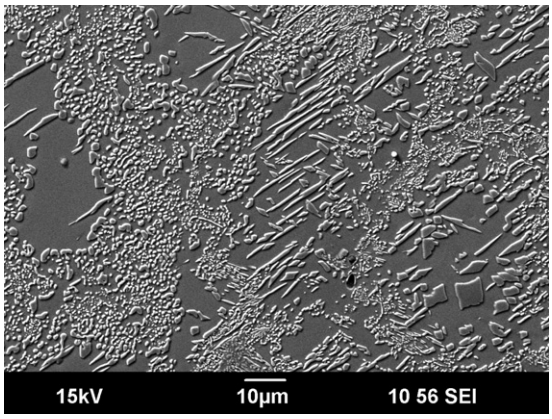

Fig. 3. Scaninng electron micrograph showing the microstructure present in the Fe–6Al–1C alloys.

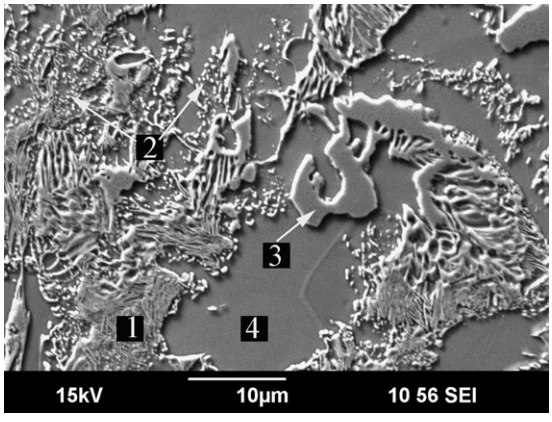

Fig. 4. Scaninng electron micrograph of the Fe–5Al–1C alloy at higher magnifications showing (1) lamellar pearlite, (2) fine spheroidal carbides, and (3) some grain boundaries carbides in a matrix of ferrite (4).

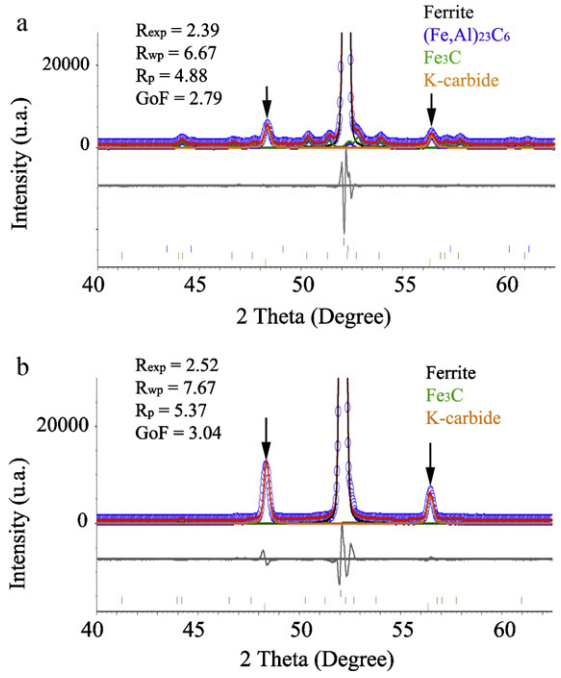

Fig. 5. Observed (hollow circles) and Rietveld fitted (solid line) X-ray diffraction patterns for (a) Fe–4Al–1C and (b) Fe–6Al–1C alloys. The difference between the experimental data and the fitted simulated pattern is shown as a continuous line under the diffraction patterns.

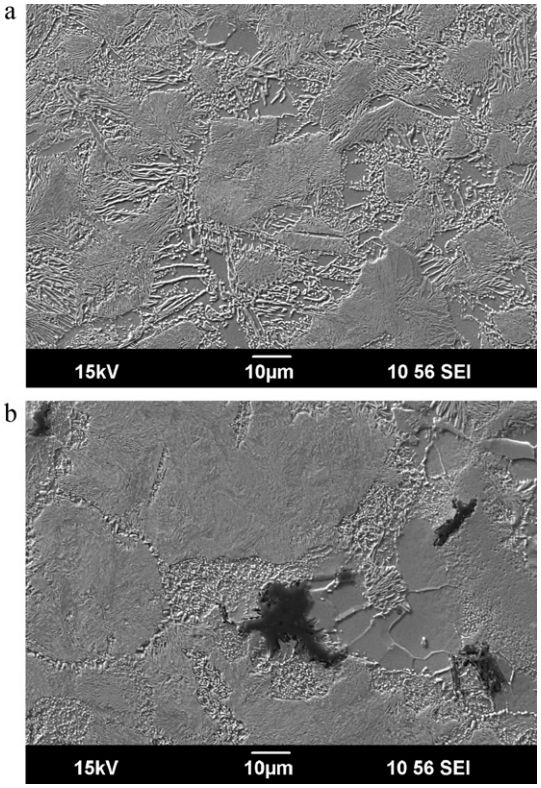

Fig. 6. Scaninng electron micrograph showing the microstructure present in (a) Fe–6Al–1.2C, and (b) Fe–6Al–1.8C alloys.

3.3. Fe–6Al–1.2C, Fe–6Al–1.4C and Fe–6Al–1.8C

Microstructure of Fe–6Al–1.2C, Fe–6Al–1.4C, and Fe–6Al–1.8C alloys consists basically of fine pearlite and some free ferrite, as shown in Fig. 6. For these alloys, pearlite consisted of alternating lamellae of ferrite and undissolved κ-carbides. Beside, graphite nodules (spherulites) surrounded by free ferrite are observed in the steels with 1.4 and 1.8 wt.% C, as observed in Fig. 6b for the Fe–6CAl–1.8C. Semiquantitative microanalysis performed in κ-carbides showed a Fe/Al atomic ratio near to 3 for the three alloys.

Table 2 shows the results of the Rietveld analysis. Similar results were obtained for the three alloys. Only some amount of graphite was observed in the alloys with 1.4 and 1.8%C.

4. Discussion

Ternary Fe–XAl–1C (with $X \leq 4$ wt.%) alloys should contain the thermodynamically stable phases α + graphite. Phase equilibria of the Fe–Al–C ternary system have been calculated using the CALPHAD approach in previous works [23,24]. The calculated vertical sections at constant C predicts for these alloys only the presence of α + graphite at temperatures below 750 °C. However, metastable Fe_3C, $(Fe,Al)_{23}C_6$ and κ-carbides were observed in the X-ray diffraction patterns due to kinetic considerations. The difficulty of obtaining information on metastable equilibria, or on unknown phases is intrinsic to the CALPHAD since the thermodynamic parameters from this method can only be evaluated from experimental data. A hypoeutectoid microstructure with some grain boundaries carbides was observed for these alloys, as shown in Fig. 1. Grain boundaries carbides are rejected at prior austenitic grain boundaries from solid solution on air cooling up to the eutectoid reaction temperature. Concentration of C in solution decrease to a hypoeutectic composition and a structure consisting of equiaxed ferrite, pearlite and some grain boundaries carbides is observed.

A binary Fe–C alloy with 1 wt.% C should present a hypereutectoid microstructure, that contain proeutectoid cementite plus pearlite. Then, grain boundaries and pearlite carbides must be different type of carbides in Fe–Al–C alloys. EDS semiquantitative microanalysis confirmed that Fe/Al atomic ratio in pearlite when the Al content is ≤4 wt.% is lower than that measured in both, ferrite and grain boundaries carbides. Considering the error associated to those measurements and that for binary Fe–C the mass fraction of ferrite in pearlite is 89%, it was concluded that pearlitic carbides almost do not contain Al. On the other hand, Fe/Al atomic ratio in grain boundaries carbides increase considerably in the alloy with 4 wt.%. For this alloys, Table 2 shows a decrease of $M_{23}C_6$ carbide content, which can be explained by the appearance of κ-carbide. Thus, grain boundaries carbides must correspond to $M_{23}C_6$ and/or κ-carbides. Cementite is contained in pearlite, and substitution of Al into cementite is not favoured.

For higher Al content, the addition of Al suppress the formation of metastable Fe_3C and $(Fe,Al)_{23}C_6$ carbides. As shown in Table 2, κ-carbides mass fraction increases from 14 to about 26% when the C content is increased. Al alters the thermodynamic constitution of the Fe–C system, and in Fe–6Al–YC alloys the pearlitic microstructure is obtained *via* quasi-eutectoid reaction: austenite → ferrite + κ-carbide. Although the carbon content is higher than in a eutectoid steel, Fig. 3 shows a typical hypo-eutectoid microstructure for the Fe–6Al–1C alloys. This alloy content 1 wt.% C and a κ-carbide mass fraction of 14%. Thus, C content and κ-carbide mass fraction in a eutectoid-like Fe–Al–C alloy are higher than carbon content and cementite mass fraction in a eutectoid binary Fe–C (0.76 and 11%, respectively). Almost a full lamellar microstructure is observed in Fig. 6a for the alloy with 1.2 wt.% C. Therefore, a relatively small amount more of C would be needed to form a pearlitic alloy through the eutectoid-like reaction from a high temperature austenite. Considering the error associated to Rietveld refinement, Table 2 shows the same concentration of κ-carbides in Fe–6Al–1.4C

Table 3
Comparison between the lattice parameter of ferrite obtained from the Rietveld refinement and calculated from the amount of Al remaining in the matrix.

Alloy	wt.%	at.%	a_{Teor}	a_{exp}
Fe–2Al–1C	2.08	4.21	2.874	2.875
Fe–3Al–1C	3.23	6.46	2.878	2.878
Fe–4Al–1C	3.83	7.62	2.880	2.881
Fe–5Al–1C	4.32	8.55	2.882	2.882
Fe–6Al–1C	4.91	9.66	2.883	2.883
Fe–6Al–1.2C	3.65	7.27	2.879	2.881
Fe–6Al–1.4C	3.41	6.81	2.878	2.880
Fe–6Al–1.8C	3.53	7.04	2.879	2.881

and Fe–6Al–1.8C alloys. As shown in Fig. 6a and b microstructure of a few graphite nodules surrounded by free ferrite in a matrix of pearlite was obtained in both alloys. The excess of C from the quasi-eutectoid composition precipitates as graphite from austenite grain boundary instead forming a network of κ-carbides, as observed in hypereutectoid steels. The graphitizing action of Al in Fe–C alloys has been reported in previous works [16]. From the maximum value of κ-carbides mass fraction in the microstructure (26%) and the formula deduced from the Rietveld analysis for κ-carbides ($Fe_3AlC_{0.8}$) it was calculated that a fully peartilic alloy should contain 1.22 wt.% of C.

An increase of carbon content determines an increase of the lattice constant of κ-carbides. In the present work, it measures an increase from 0.3784 to 0.3790 when in the compound Fe_3AlC_x the value of x increases from 0.8 to 1. Several authors have found a linear relationship between the lattice constant value and carbon content in atomic percent [14,18]. Although there is obviously some spread about the ideal ratio Fe:Al corresponding to Fe_3Al, it has been reported that the lattice constant of κ-carbides is mainly controlled by the carbon content [14]. EDS semiquantitative microanalysis confirmed that Fe/Al atomic ratio close to 3 for the κ-carbides present in the studied alloys. From a linear refinement of lattice constants and carbon content determined in the Rietveld refinement (Table 2) and the value of 0.378 nm reported by Huetter et al. for $x = 0.66$ [16], the dependence of the lattice constant on the carbon content was determined as:

$$a_{\kappa\text{-carbide}} = 0.37605 + 0.00295\,\text{at.\%C} \quad (1)$$

The lattice parameter of ferrite and the Al content in solution has been correlated in several studies [25]. The rate of lattice parameter increase at room temperature appears to be linear up to ~15 at.%:

$$a_{\text{ferrite}} = 0.28660 + 0.00018\,\text{at.\%Al} \quad (2)$$

A higher ferrite lattice parameter in Table 2 indicates an increase of Al solute concentration in ferrite. On the other hand, the values of a_{ferrite} deduced from the Rietveld refinement can be checked introducing the Al content in the ferrite in Eq. (2). Considering that all C are forming carbides and the results of mass fraction of Table 2, it was calculated the amount of Al remaining in the matrix. These values were introduced in Eq. (2) to obtain the corresponding the lattice parameter. As shown in Table 3 a good correlation between both, measured and calculated a_{ferrite} was obtained.

5. Conclusions

The combination of microstructure characterization and Rietveld refinement method to analyse XRD spectra has been proven an effective method to obtain detailed information about the carbides present in ternary Fe–Al–C. Presence of metastable carbides is controlled mainly by the Al content but also by the carbon concentration:

(a) The alloys with an Al content ≤ 4 wt.% present a structure consisting of equiaxed ferrite, ferrite + Fe_3C pearlite and some grain boundaries $M_{23}C_6$ and/or κ-carbides. It is the first time that the existence of a $M_{23}C_6$ ternary carbide in the Fe–Al–C has been recognized. On the other hand, the amount of Al in the cementite is negligible and hence the lattice parameter does not depend on the Al concentration of the alloy.
(b) The formation of metastable Fe_3C and $(Fe,Al)_{23}C_6$ carbides is suppressed for an Al content higher than 5 wt.%. The pearlitic microstructure in Fe–6Al–YC alloys is obtained *via* quasi-eutectoid reaction: austenite → ferrite + κ-carbide.
(c) A fully quasi-eutectoid Fe–6Al–YC pearlitic alloy should contain 1.22 wt.% of C. The excess of C from this value forms graphite nodules instead forming a network of κ-carbides at the prior austenitic grain boundaries.

Acknowledgement

This work was supported by the Comisión Interministerial de Ciencia y Tecnología (CICYT), Spain, under Grant MAT2009-14385.

References

[1] T. Mishima, N. Makino, Tetsu-to-Hagane 43 (1957) 556–560.
[2] J.J. Wyslocki, J. Olszewski, S. Szymura, Mater. Chem. Phys. 45 (1996) 193–196.
[3] G. Frommeyer, E.J. Drewes, B. Engl, Rev. Metall. -Cah. Inf. Technol. 97 (2000) 1245–1253.
[4] J. Herrmann, G. Inden, G. Sauthoff, Acta Mater. 51 (2003) 2847–2857.
[5] W.R. Kerr, Metall. Trans. A 17 (1986) 2298–2300.
[6] R.G. Baligidad, U. Prakash, A. Radhakrishna, Mater. Sci. Eng. A 255 (1998) 162–168.
[7] R.G. Baligidad, A. Radhakrishna, Mater. Sci. Eng. A 283 (2000) 211–217.
[8] W. Sanders, G. Sauthoff, Intermetallics 5 (1997) 361–375.
[9] W. Sanders, G. Sauthoff, Intermetallics 5 (1997) 377–385.
[10] F.R. Morral, J. Iron Steel Inst. 130 (1934) 419–428.
[11] K. Nishida, Bulletin of the Faculty of Engineering, vol. 48, Hokkaido University, 1968, pp. 71–108.
[12] K. Loehberg, A. Ueberschaer, Giessereiforschung 21 (1969) 171–173.
[13] V. Raghavan, J. Phase Equilib. 14 (1993) 615–617.
[14] M. Palm, G. Inden, Intermetallics 3 (1995) 443–454.
[15] G. Ghosh, in: G. Effenberg, S. Ilyenko (Eds.), Ternary Alloy Systems–Phase Diagrams, Crystallographic and Thermodynamic Data: Light Metal Systems, Part 1: Selected Systems from Ag–Al–Cu to Al–Cu–Er, Landolt-Börnstein, New Series IV/11A1, MSI Materials Science International Services GmbH/SpringerMaterials, Berlin/Heidelberg, 2004, pp. 123–138.
[16] L.J. Huetter, H.H. Stadelmaier, Acta Metall. 6 (1958) 367–370.
[17] P.J. James, J. Iron Steel Inst. 207 (1969) 54–57.
[18] W.K. Choo, K.H. Han, Metall. Trans. A 16 (1985) 5–10.
[19] V.K. Pecharsky, P.Y. Zavalij, Fundamentals of Powder Diffraction and Structural Characterization of Materials, Springer, New York, 2005.
[20] I.R. Shein, N.I. Medvedeva, A.L. Ivanovskii, Physica B 371 (2006) 126–132.
[21] H.L. Yakel, Acta Crystallogr. B 43 (1987) 230–238.
[22] J. Xie, J. Shen, N. Chen, S. Seetharaman, Acta Mater. 54 (2006) 4653–4658.
[23] D. Connetable, J. Lacaze, P. Maugis, B. Sundman, CALPHAD 32 (2008) 361–370.
[24] H. Ohtani, M. Yamano, M. Hasebe1, ISIJ Int. 44 (2004) 1738–1747.
[25] F. Lihl, H. Ebel, Arch. Eisenhüttenwes. 32 (1961) 483–487.